Article

Probing the Physicochemical Behavior of Variously Doped $Li_4Ti_5O_{12}$ Nanoflowers

Kenna L. Salvatore, Mallory N. Vila, Genesis Renderos, Wenzao Li, Lisa M. Housel, Xiao Tong, Scott C. McGuire, Joceline Gan, Ariadna Paltis, Katherine Lee, Kenneth J. Takeuchi, Amy C. Marschilok, Esther S. Takeuchi, and Stanislaus S. Wong*

Cite This: *ACS Phys. Chem Au* 2022, 2, 331–345

Read Online

ACCESS | 📊 Metrics & More | 📖 Article Recommendations | SI Supporting Information

ABSTRACT: This study thoroughly investigated the synthesis of not only 4 triply-doped metal oxides but also 5 singly-doped analogues of $Li_4Ti_5O_{12}$ for electrochemical applications. In terms of synthetic novelty, the triply-doped materials were fabricated using a relatively facile hydrothermal method for the first-time, involving the simultaneous substitution of Ca for the Li site, Ln (i.e., Dy, Y, or Gd) for the Ti site, and Cl for the O site. Based on XRD, SEM, and HRTEM-EDS measurements, the resulting materials, incorporating a relatively homogeneous and uniform dispersion of both the single and triple dopants, exhibited a micron-scale flower-like morphology that remained apparently undamaged by the doping process. Crucially, the surface chemistry of all of the samples was probed using XPS in order

to analyze any nuanced changes associated with either the various different lanthanide dopants or the identity of the metal precursor types involved. In the latter case, it was observed that the use of a nitrate salt precursor versus that of a chloride salt enabled not only a higher lanthanide incorporation but also the potential for favorable N-doping, all of which promoted a concomitant increase in conductivity due to a perceptible increase in Ti^{3+} content. In terms of the choice of lanthanide system, it was observed via CV analysis that dopant incorporation generally (albeit with some notable exceptions, especially with Y-based materials) led to the formation of higher amounts of Ti^{3+} species within both the singly and triply-doped materials, which consequentially led to the potential for increased diffusivity and higher mobility of Li^+ species with the possibility for enabling greater capacity within these classes of metal oxides.

KEYWORDS: lithium titanate, doping, nanomaterials, spectroscopy, electrochemistry, lithium ion battery, hydrothermal synthesis, electrochemical tuning
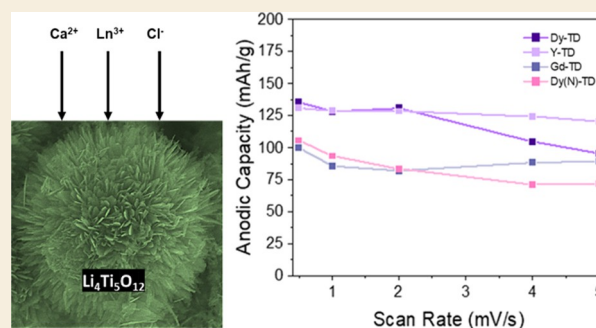
1. INTRODUCTION

Lithium titanate ($Li_4Ti_5O_{12}$, LTO) has been well studied for its potential use as a viable lithium-ion battery (LIB) anode.[1–3] In effect, LTO benefits from a "zero strain" structure; its distinctive spinel crystal structure promotes not only an increased electrode stability during the lithiation/delithiation processes but also a high thermal stability, all of which are definitely highly desirable attributes. Furthermore, LTO is also an advantageous material due to its highly stable discharge/ charge voltage plateau of 1.55 V vs Li^+/Li, which lies above the relevant electrolyte reduction potentials. Hence, LTO is conducive to either reducing or preventing the formation of a solid electrolyte interphase (SEI) layer. On the other hand, LTO suffers from both low intrinsic conductivity[1] ($10^{-13}–10^{-9}$ S/cm) in addition to sluggish Li diffusion kinetics, all of which can hinder its overall applicability.[4]

To mitigate these limitations, the strategy of doping represents a well-studied approach for not only increasing the conductivity of LTO but also enhancing its Li^+ diffusion kinetics.[1] As such, a large number of different elements have been individually doped into the LTO matrix (Table S1). Moreover, elements can be co-doped with one another either onto the same site or at different sites (Table S1) such that one can potentially take advantage of the full range and permutation of distinctive varieties and types of sites with which to dope. Specifically, as we will discuss, the presence of introduced dopants can favorably impact not only the electronic and ionic conductivity but also the corresponding Li ion diffusion properties of LTO-based materials. Moreover, the presence of co-dopants can yield improved rate capacity
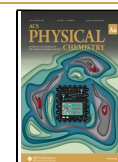
and rate stability and introduce novel functionalities, as compared with their singly-doped counterparts.

In effect, there are various types of dopants that can be probed. Some studies have investigated the insertion of two chemically distinctive elements to target two correspondingly different elements. One example is Ca^{2+} substituting at the Li^+ site with Sm^{3+} localizing at the Ti^{4+} site; this co-doping protocol apparently improved not only reversibility but also Li^+ diffusion.[5] Other groups have analyzed the concept of either (i) using one element to dope two different sites, such as the simultaneous localization of Cr^{3+} into both Li^+ and Ti^{4+} sites,[6] or (ii) the use of two dissimilar elements to dope into one singular site, with an illustrative example of Na^+ and K^+ both co-doped into the Li^+ site.[7] Moreover, past work has shown that the introduction of co-dopants into the LTO lattices does not necessarily lead to any observable changes in the physical structure, though these species have been known to increase not only electronic conductivity but also Li^+ diffusion.[8] For instance, when Mg^{2+} and La^{3+} were co-doped into the Li^+ and $Ti^{3+/4+}$ sites, the resulting material exhibited a discharge capacity of 107.8 mAh·g^{-1} after 500 cycles. This novel doubly-doped motif yielded an improved performance as compared with not only their singly-doped counterparts but also bare LTO. Specifically, capacity values of 75.2, 85.3, and 55.6 mAh·g^{-1} were measured after 500 cycles for Mg-doped LTO, La-doped LTO, and pure LTO, respectively.[9] Complementary DFT analysis was consistent with not only an enhanced electrochemical performance but also an improved electronic conductivity.[9]

However, there have been few systematic studies on the doping of metal oxides in general for electrochemical applications and virtually no studies on the "triple doping" of LTO in particular. Nevertheless, the concept of "triple doping" has previously been applied to various metal oxide species, including but not limited to titanium dioxides[10] and perovskite oxides;[11] these reports implied that such an unusual doping strategy led to better-quality solar conversion properties due to both an increase in electron transfer as well as an improved chemical stability. As an example, in the case of $LiNi_{0.5}Mn_{1.5}O_4$ used as a cathode for LIBs, the base material was triply doped with Cu^{2+}, Al^{3+}, and Ti^{4+}. The net product exhibited not only an enhanced electronic conductivity that increased from 0.77×10^{-5} to 2.58×10^{-5} S/cm but also an improved Li^+ diffusion, all of which led to positive consequences for its electrochemical performance; indeed, the doped sample maintained an enhanced specific capacity of ~101 mAh·g^{-1} at 100 C.[12]

As such, to the best of our knowledge, the work herein presents a thorough investigation, for the first time, of the "triple doping" of LTO using a facile and high-yield hydrothermal method, previously developed by this group.[4] Specifically, as relevant prior studies and justification for our approach, we have previously demonstrated in LTO systems that (a) Ca^{2+} can successfully substitute into the Li^+ site,[13] and separately, that (b) Cl^- can be inserted into the O^{2-} site.[4] As an added level of sophistication, our group improved upon the intrinsic stability of LTO by rational morphological manipulation by either (i) using a micron-scale "flower-like" morphology or (ii) combining LTO with carbon nanotubes. To these LTO motifs, we initiated doping of LTO at the Li site and the O site with Ca^{2+} and Cl^-, respectively (Table S2).[4,13,14]

When cationic doping with Ca^{2+}, a higher rate capability was measured with superior cycling stability in addition to an increase in electronic conductivity, all of which was attributed to the partial reduction of Ti^{4+} to Ti^{3+} (Table S2).[13] Indeed, within $Li_{4-x}Ca_xTi_5O_{12}$ systems, when the Ca doping amount attained a level of "x" = 0.2, a corresponding increase in the Li diffusion coefficient was observed at 4.6×10^{-13} cm^2·s^{-1} with a specific measured capacitance of 151 and 143 mAh·g^{-1} under discharge rates of 20 C and 40 C at cycles 60 and 70, respectively. Other studies regarding the use of Ca have noted similar trends regarding the synergistic increase in Li diffusion and capacitance.[15,16] With analogous anionic Cl^- doping in the context of $Li_4Ti_5O_{11.5}Cl_{0.5}$, similar types of results were observed with the partial reduction of Ti, which yielded not only an improvement in electronic conductivity but also a 12% increase in capacity from an initial value of 182 mAh·g^{-1} at 0.2 C as compared with their undoped counterparts (Table S2). Additionally, in both cases, the sheer quantity of dopant was optimized so as to increase electronic conductivity, rate capacity, and rate stability, while simultaneously maintaining structure, underlying morphology, and overall chemical composition.

In this report, we chose 4f lanthanide metals to be substituted into the Ti site, because these metal ions are known to promote an increase in both cycling performance and rate capacity. Specifically, for this study, lanthanide ions, such as Dy^{3+}, Y^{3+}, and Gd^{3+}, were selected as the dopant for the Ti site, because of prior literature precedence for the use of these elements. For example, Dy^{3+} has been already reported as both a single dopant and a co-dopant for $Ti^{3+/4+}$ and $Li^+/Ti^{3+/4+}$ sites, respectively (Table S2).[17,18] In particular, using a hydrothermal-based synthesis, $Li_{4-x/3}Ti_{5-2x/3}Dy_xO_{12}$, wherein "$x$" = 0.02, was found to exhibit a specific discharge capacity of 181.8 mAh·g^{-1} at 20 C and 140.9 mAh·g^{-1} after 1000 cycles, even at 100 C within a potential range from 0.01 to 2.5 V, representing a capacity higher than its theoretical value.[17] Similarly, Gd^{3+} has also been noted as both a single and co-dopant for $Ti^{3+/4+}$ and $Li^+/Ti^{3+/4+}$ sites, respectively.[19−21] It was observed that the presence of Gd^{3+} did not change the spinel structure but rather improved the rate capability and cycling stability while only allowing for a small amount of these ions to enter the lattice.[20,21] As an illustrative example, a hydrothermally derived Gd-doped LTO sample displayed higher discharge capacities than that of the theoretical capacity with measured values of 213, 182, 171, and 146 mAh·g^{-1} obtained at rates of 1, 5, 10, and 30 C, respectively, coupled with a Li diffusion coefficient of 1.83×10^{-11} cm^2·s^{-1} after 100 cycles.[21] Furthermore, the use of Y^{3+} doping also led to enhanced electronic and ionic conductivities in addition to a greater cycling stability.[22,23] As an instructive example, Y^{3+}-doped $Li_4Ti_5O_{12}$ (Y_xLTO, x = 0.06), emanating from a co-precipitation reaction, was characterized by a reversible capacity of 141.3 mAh·g^{-1} for "x" = 0.06 after 1800 cycles at 10 C in conjunction with a Li diffusion coefficient of 6.69×10^{-12} cm^2·s^{-1}.[22] Both of the studies probing Gd and Y doping mentioned that excess dopant incorporation, i.e., above a 0.1 mol dopant to 1 mole of LTO ratio, could lead to a distortion of the underlying LTO lattice, thereby decreasing the measured electrochemical performance.[22]

It is worth highlighting that the ionic radius of Dy^{3+}, Y^{3+}, and Gd^{3+} has been determined to be 91.2,[17] 90,[22] and 93.8 pm,[21] respectively. These values are much larger than the corresponding ionic radii for Li^+ (76.0 pm) and Ti^{4+} (60.5 pm).[17] As such, given these geometric and spatial constraints, the actual quantitative incorporation of lanthanide ions within

LTO is a significant parameter that needs to be optimized. As such, our "triple-doping" protocol seeks to not only study the effects of incorporating all 3 distinctive doping entities (i.e., Ca^{2+}, Cl^-, and a given lanthanide ion) but also assess how the doping process itself impacts the observed electrochemical behavior of these chemically modified materials. Along this line of thought, we have also analyzed the effect of the identity of the metal salt used, because previous studies have implied that doping can originate from the anion of an organic salt.[4] Hence, two different metal salts associated with lanthanide precursors will be investigated to discern either (i) any perceptible differences between the effects of these two reagents or (ii) if the anion is found to also participate in the doping process during this reaction.

To summarize, this paper aims for the first time to synthesize a novel "triply-doped" LTO system. In the process, we probe not only the metal salt identity but also the choice of lanthanide in potentially regulating electrochemical performance. These data should prove to be useful for understanding the behavior of not only LTO dopant species in particular but also metal oxide dopants in general. As such, this study aims to correlate observed electrochemistry with rational, deterministic changes to dopant structure and composition, utilizing a suite of complementary characterization techniques, such as XRD, SEM, HRTEM-EDS, and XPS.

2. EXPERIMENTAL SECTION

2.1. Hydrothermal Synthesis of Precursor Li4Ti5O12 Nanoflowers

The following hydrothermal method was based upon a previously published protocol.[4] In this regard, a 50 mL aqueous solution of 0.40 M LiOH (Acros Organics, 98%) was stirred within a 120 mL autoclave. Upon dissolution of LiOH, 2.5 mL of 30% (w/w) H_2O_2 (VWR) aqueous solution was subsequently inserted into the above aqueous solution dropwise, followed by stirring for 5 min. The titanium-containing precursor, titanium butoxide (TBOT, Alfa Aesar, 99 + %), was slowly dripped into the solution (1.7 mL, 5 mmol) with stirring for 3 h. Upon placement of the solution mixture within a steel autoclave, the apparatus was heated for 36 h at 130 °C. The as-prepared white precipitate product was washed with ethanol for 3 times prior to a final annealing step within a tube furnace at 500 °C for 3 h using a ramp rate set at 3 °C per minute.

2.2. Hydrothermal Synthesis of Singly-Doped Li4Ti5O12 Nanoflowers

Control samples consisting of singly-doped LTO material were generated based on minor variations of a prior published hydro-thermal method by this group.[4] This represented a reasonably familiar modus operandi, considering that we have chemically modified LTO with these individual types of species in our previous body of work. We employed hydrothermal syntheses for all of these runs while altering only the precursor compositions and concentrations.

2.2.1. Ca-Doped Li4Ti5O12 Nanoflowers. As such, for the Ca-doping experiments, i.e., cation doping, an initial precursor solution of 2 M Ca(acetate)$_2$·H_2O (Sigma Aldrich, 99%) was created. For 0.2 mmol Ca-doped LTO (singly-doped Ca-SD), as previously optimized for these types of experiments,[13] ∼0.1 mL of this solution was put into an aqueous LiOH solution, prior to the addition of H_2O_2 and TBOT.

2.2.2. Cl-Doped Li4Ti5O12 Nanoflowers. Similarly, for the Cl-doping experiments, i.e., anion doping, a precursor solution of 5 M NH_4Cl (Alfa Aesar, 98 + %) was produced. Based on previous studies, for 0.5 mmol Cl-doped LTO (singly doped "Cl-SD"), an amount previously optimized for these types of experiments,[4] ∼0.1 mL of this solution was inserted in an aqueous LiOH solution, before the addition of H_2O_2 and TBOT.

2.2.3. Singly Ln-Doped Li4Ti5O12 Nanoflowers. With respect to lanthanides, we chose to analyze Dy, Y, and Gd. In separate experiments, we prepared 0.6 M precursor solutions, spanning the range of lanthanide species of Dy, Y, and Gd. Specifically, the relevant lanthanide-containing precursors we used included $DyCl_3$ (Alfa Aesar, 98 + %), $Dy(NO_3)_3$·$5H_2O$ (Alfa Aesar, 99.9%), $Y(NO_3)_3$ (Alfa Aesar, 98 + %), and $Gd(NO_3)_3$·H_2O (Alfa Aesar, 99.9 + %) for the individual experiments we reported herein. For the variously doped samples, we generated each of the discrete, metal-ion-containing solutions at nominal quantities of 0.06 mol, a value chosen based on prior literature experiments, which had optimized this very amount.[13] Subsequently, ∼0.1 mL of the lanthanide ion-containing solution was added into the LiOH medium, prior to the addition of H_2O_2 and TBOT. In so doing, we were able to fabricate a series of singly-doped (SD) LTO samples, comprising these heavy metals. These included (i) Dy-containing "Dy-SD" using the chloride salt precursor and (ii) "Dy(N)-SD" utilizing the nitrate salt precursor; (iii) Y-containing "Y-SD" using $Y(NO_3)_3$; and (iv) Gd-containing "Gd-SD" in the presence of $Gd(NO_3)_3$, encapsulating the targeted lanthanide species.

2.3. Hydrothermal Synthesis of Triply-Doped Li4Ti5O12 Nanoflowers

A triply-doped (TD) analogue of the LTO material was prepared based on a previously published hydrothermal method by this group.[4] Specifically, the triply-doped samples were generated identically to that of the singly-doped variants. The sole difference was that in our experiments, all three of the intended dopants were systematically added to the same solution, i.e., the same reaction "pot", prior to the introduction of H_2O_2 and of TBOT.

In so doing, we fabricated a distinctive, triply-doped series with nitrate-based precursors, consisting of not only (i) Ca, Y, and Cl-doping but also (ii) Ca, Gd, and Cl-doping, representing the Y- and Gd-containing samples, respectively. Moreover, to probe the role of the nature of the precursor identity within a set of Dy-containing samples, we investigated whether using the chloride or the nitrate analogue of the Dy salt made any difference. Therefore, we created a series of analogous samples associated with Ca, Dy, and Cl-doping, with either $DyCl_3$ or $Dy(NO_3)_3$·$5H_2O$; as such, these samples are referred to herein as being based on "Dy" and "Dy(N)", respectively. In total, four triply-doped (TD) LTO-based samples were investigated: (i) Ca, Dy, Cl −LTO, denoted as "Dy-TD"; (ii) Ca, Y, Cl-LTO, designated as "Y-TD"; (iii) Ca, Gd, Cl-LTO, labeled "Gd-TD"; and (iv) Ca, Dy(N), Cl-LTO, otherwise indicated as "Dy(N)-TD".

2.4. Structural Characterization Techniques and Methodology

2.4.1. XRD. The series of relevant doped LTO samples were prepared by dispersion of the isolated precipitate in ethanol and then drop-casting that mixture several times onto a zero-background holder (MTI Corporation, zero diffraction plate for XRD, B-doped, p-type Si, measuring 23.6 mm in diameter by 2 mm in thickness). Diffraction pattern data were then collected with a Rigaku Miniflex diffractometer, operating in the Bragg configuration. Results for the individual, discrete samples were separately acquired using Cu $K\alpha_1$ irradiation (λ = 1.54 Å) across the range of 10° to 60° with a scanning rate at 5° per minute. Approximate average crystallite sizes were computed using the Scherrer equation (Table S3).

2.4.2. Electron Microscopy Imaging. An ultrahigh-resolution field emission Hitachi 4800 scanning electron microscope was utilized to characterize the apparent morphology of the as-prepared structures. Specifically, both the pristine and the corresponding series of variously doped LTO samples were dispersed in ethanol and subsequently drop cast onto a silicon wafer. Associated HRTEM samples were prepared by drop-casting aliquots of a LTO suspension in ethanol onto a carbon-coated copper grid. The HRTEM analysis was performed on a JEOL 2100F, run using an accelerating voltage of 200 kV. Additional images were acquired in the scanning transmission electron microscopy (STEM) mode.

2.4.3. X-ray Photoelectron Spectroscopy (XPS). X-ray photoelectron spectroscopy enables insights into elemental composition and oxidation state information for the different elements within our samples. In preparing SEM samples, product powders were dispersed in ethanol and then drop cast onto an underlying Si wafer (1 cm × 1 cm). The suite of XPS experiments was initiated using a home-made system, with a model SPECS Phoibos 100 electron energy analyzer for electron detection. Al Kα radiation (1486.6 eV) (model XR 50) was utilized as the X-ray source, during the data collection algorithm. Spectra associated with the Ti 2p in addition to the doping regions of interest herein, namely, Cl 2p, N 1s, Gd 4d, Dy 4d, Y 3d, and Ca 2p, respectively, were processed. Signals ascribed to the lanthanides, namely, Ca 2p, Cl 2p, and N 1s were analyzed using a Tougaard background correction and the Ti 2p region was interpreted using a Shirley background correction. Raw areas are compiled in Table S4 with the formulae for relative area calculations provided in Formula S1.

2.4.4. Electrochemistry. The electrochemical behavior of the samples was assessed using cyclic voltammetry. Electrodes were prepared as foil coatings by mixing the LTO samples with carbon and polyvinylidene fluoride (PVDF) in an 85:10:5 weight ratio. These mixtures were subsequently cast onto aluminum foil. The requisite coin cells were assembled using Li metal foil in an electrolyte, comprising 1 M LiPF$_6$ in a 3:7 (vol:vol) ethylene carbonate and dimethyl carbonate mixture under inert conditions. Cyclic voltammetry data were collected using a potentiostat wherein the lithium anode was considered as both the reference electrode and the counter electrode. Cyclic voltammetry data were acquired using a voltage range of 1.0 to 3.0 V and scan rates of 0.5, 1.0, 2.0, 4.0, and 5.0 mV s^{-1}. Galvanostatic cycling data were collected for 20 cycles at 0.2C between 1.0 and 2.5 V.

3. RESULTS AND DISCUSSION

3.1. Characterization of Li$_4$Ti$_5$O$_{12}$ Singly and Triply-Doped Samples

A series of singly-doped Li$_4$Ti$_5$O$_{12}$ (LTO) samples were initially produced as baseline materials for comparison, namely the Ca-SD, Dy-SD, Y-SD, Gd-SD, Dy(N)-SD, and Cl-SD series. The single dopant ions were individually tested. Based on prior work, the corresponding anticipated destinations were thought to be Cl$^-$ for the anionic O^{2-} site, Ca^{2+} for the Li$^+$ site, and a range of lanthanide ions, including Gd^{3+}, Dy^{3+}, and Y^{3+}, for the Ti^{4+} site, respectively. Moreover, we also investigated the use of two different types of metal salts, specifically DyCl$_3$ (Dy-SD) and Dy(NO$_3$)$_3$ (Dy(N)-SD), in order to determine the effect, if any, of the identity of the counteranion salt upon the composition and morphology of the resulting sample. In particular, we sought to determine if the anion was serving as an added quantitative dopant within the LTO matrix. Therefore, our overall goals were to determine (i) if single dopant insertion into the LTO matrix could be successfully initiated, (ii) if there were any apparent impurities within the sample, and (iii) if the micron-scale "flower-like" morphology tended to be conserved after the reaction process.

Additionally, the creation of triply-doped LTO species was manifested in the production of 4 different types of samples, i.e., Dy-TD, Y-TD, Gd-TD, and Dy(N)-TD. Over the course of our studies, we have found that Ca was consistently substituting at the Li site, whereas Cl was analogously localizing at the O site. What we varied and were most concerned about analyzing was the nature of the lanthanide involved (i.e., Gd, Y, or Dy) in addition to the effect of varying precursor identity (i.e., Dy chloride versus Dy nitrate). The doping amounts for each triply-doped sample remained

identical to that utilized to generate their respective singly-doped LTO analogues.

3.1.1. XRD Analysis. As observed from the X-ray diffraction (XRD) patterns in Figure 1A, there is no obvious
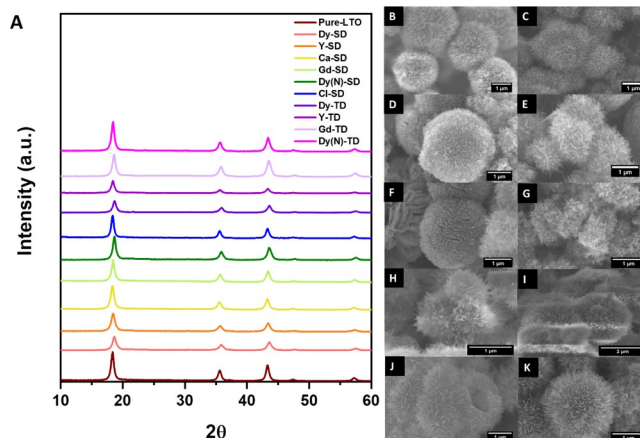

Figure 1. (A) XRD patterns of pure LTO (maroon). Analogous data on the corresponding doped analogues of a series of singly-doped materials (i.e., Dy-SD (red), Y-SD (orange), Ca-SD (yellow), Gd-SD (light green), Dy(N)-SD (green), and finally Cl-SD (blue)), in addition to their triply-doped analogues (i.e., Dy(N)-TD (pink); Gd-TD (light pink); Y-TD (light purple); and Dy-TD (purple)). Corresponding SEM images of series of not only singly-doped (B) Cl-SD, (C) Ca-SD, (D) Dy-SD, (E) Y-SD, (F) Gd-SD, and (G) Dy(N)-SD samples but also triply-doped (H) Dy-TD, (I) Y-TD, (J) Gd-TD, and (K) Dy(N)-TD samples.

appearance of impurities within either the pure LTO control (maroon) or singly-doped samples of Dy-SD (red), Y-SD (orange), Ca-SD (yellow), Gd-SD (light green), Dy(N)-SD (dark green), and Cl-SD (blue). Additionally, under conditions conducive to triple doping, it was observed that the addition of all 4 types of dopants did not lead to any obvious compositional impurities for any of the triply-doped samples, whether it be either Dy-TD (dark purple), Gd-TD (light pink), Y-TD (purple), or Dy(N)-TD (pink). These data collectively support the idea that the dopants themselves did not affect the nature of the underlying LTO matrix. Upon dopant ion insertion at these relatively low concentrations, the intrinsic LTO framework was conserved. These findings would suggest that the addition of the individual single dopant yielded a pure composition with no noticeable and apparent impurities, including but not limited to TiO$_2$ and LiTi$_2$O$_3$ species, which might otherwise have been expected to have formed.

3.1.2. Morphological Analysis. Furthermore, the morphologies of these variously doped samples were explored using scanning electron microscopy (SEM) (Figure 1B−G). Significantly, the data confirmed that the generation of singly-doped LTO samples gave rise to micron-scale, "flower-like" morphologies regardless of whether (B) Cl-SD, (C) Ca-SD, (D) Dy-SD, (E) Y-SD, (F) Gd-SD, or (G) Dy(N)-SD had been formed. That is, as we had hoped for, our series of doped counterparts are morphologically similar to that of pure, undoped, pristine LTO samples (Figure S1D).[4] By analogy with the singly doped counterparts, no clear morphological impurities were detected for any of the triply-doped materials analyzed, such as either the (H) Dy-TD, (I) Y-TD, (J) Gd-TD, or (K) Dy(N)-TD samples. All of these triply-doped-based architectures exhibited micron-scale, "flower-like" morpholo-
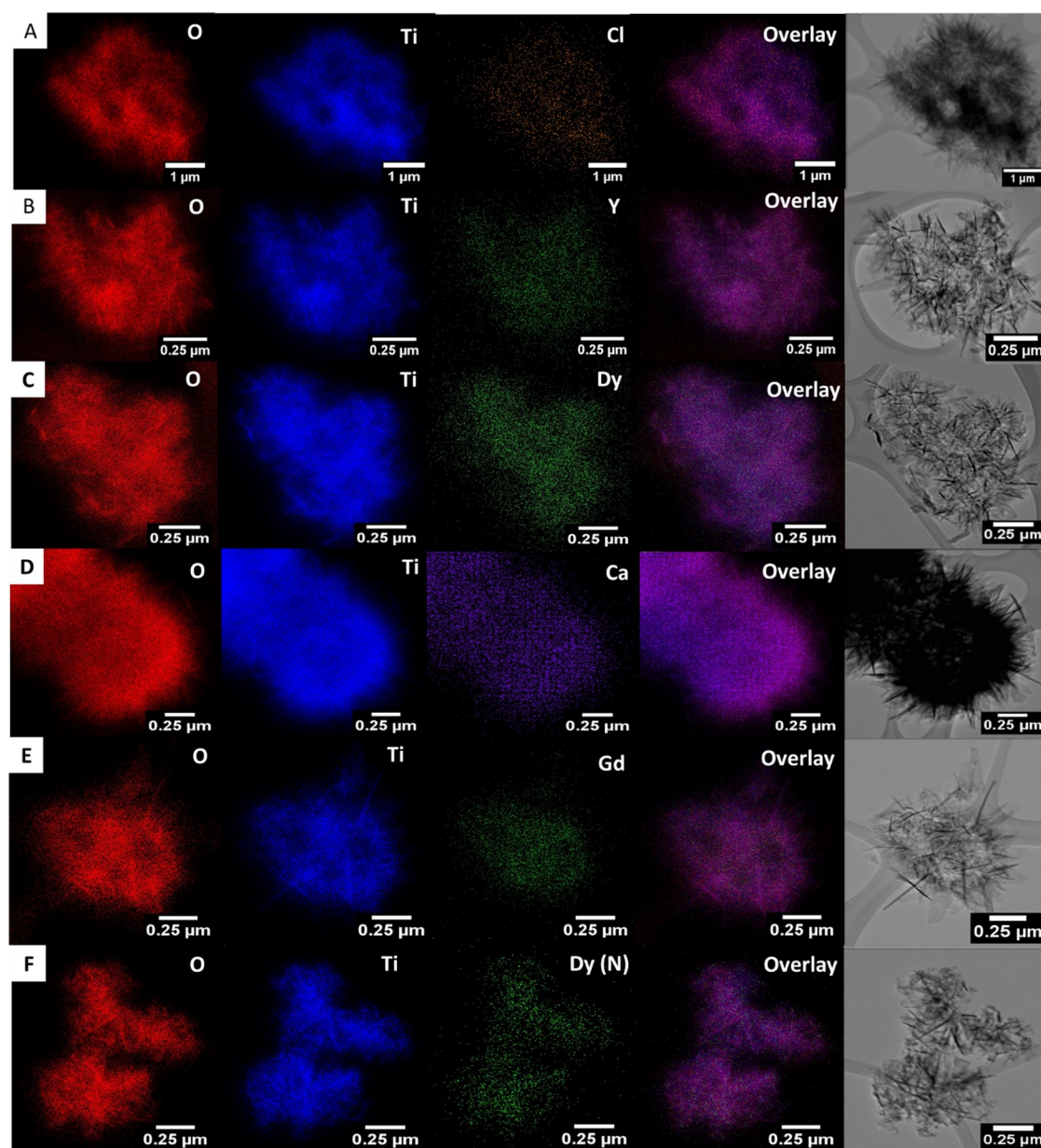
Figure 2. HRTEM-EDS mapping data and the corresponding STEM image of (A) Cl-SD, (B) Y-SD, (C) Dy-SD, (D) Ca-SD, (E) Gd-SD, and (F) Dy(N)-SD samples. Ti is marked off as blue, O is denoted as red, and the relevant dopant is either green (Ln) or purple (Ca).

gies, resembling not only singly-doped materials but also their pure LTO analogues.

Moreover, to ascertain the nature of the distribution of the desired dopant element within the sample, high-resolution transmission electron microscopy energy-dispersive spectroscopy (HRTEM-EDS) mapping was utilized to confirm a homogeneous dispersion and localization of the desired dopant throughout the entire LTO micron-scale flowers for both the singly and triply-doped materials (Figures 2 and 3, respectively). As presented in Figure 2, all of the singly doped samples exhibited a relatively uniform and regular dispersal of their respective elements, indicative of the successful insertion of the dopant within the underlying LTO matrix and the relative uniformity of the dopant distribution within the sample. Specifically, as observed in the (A) Cl-SD (B) Y-SD, (C) Dy-SD, (D) Ca-SD, (E) Gd-SD, and (F) Dy(N)-SD samples, Ti is marked off as blue, O is

denoted as red, and the relevant dopant is labeled either green (Ln) or purple (Ca). All singly-doped samples were found to exhibit a homogeneous and consistent dispersion of the relevant elements within the samples (Figure 2).

With respect to the HRTEM-EDS analysis of the triply-doped samples (Figure 3), the expected Ca and Cl elements could be readily identified. Furthermore, the individual lanthanide dopants are shown in green coloration for (A) Dy, (B) Y, (C) Gd, and (D) Dy(N), respectively. As can be concluded from the HRTEM-EDS mapping data, remarkably, the positions of the signals from all of the desired anionic and cationic dopant elements tend to be spatially coincident and overlapping with each other, with the implication that these individual elements are effectively uniformly and evenly spread out throughout the sample, as opposed to forming discrete clusters or islands. The corresponding chemical character-
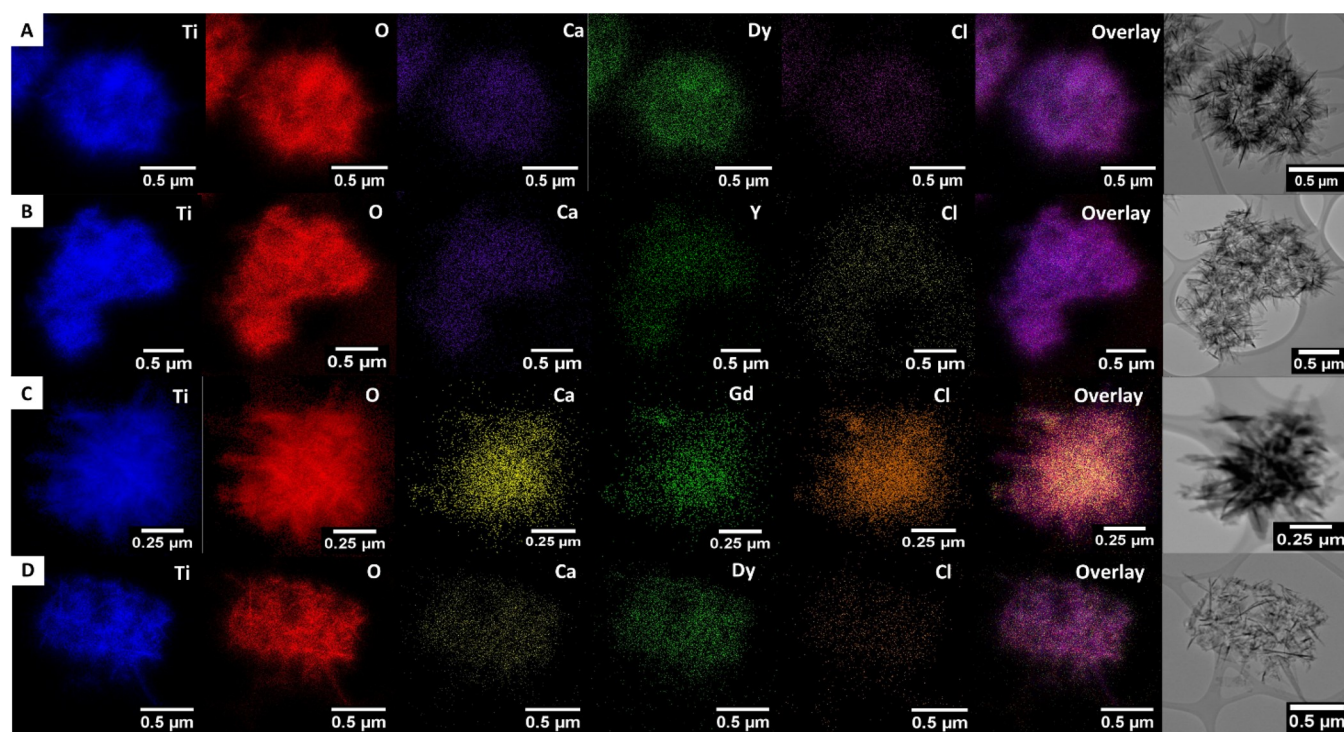
Figure 3. HRTEM-EDS mapping images of the series of triply-doped (A) Dy-TD, (B) Y-TD, (C) Gd-TD, and (D) Dy(N)-TD samples. Elements presented include Ti (blue), O (red), Ln (Dy, Y, Gd) (green), Cl, and Ca. The composite elemental overlay and associated morphological HRTEM images are shown at the far right.

ization of pure LTO (HRTEM-EDS) is presented in Figure S1 as a reference point.

3.1.3. XPS Analysis. *3.1.3.1. Analysis of the Ti 2p Region.* General Comments: It is worth highlighting that to the best of our knowledge, surface compositional analysis has not been previously reported on triply-doped lithium titanates. Hence, to emphasize the novelty of our study, X-ray photoelectron spectroscopy (XPS) was used to examine the surface chemistry of the doped materials. Initially, the Ti 2p region was evaluated for the singly-doped samples (Figure 4). The results of the analysis demonstrated that the pristine LTO sample (Figure 4A, Table S4) only gave rise to Ti^{4+} peaks (red) at 458.0 eV (Ti^{4+} $2p_{3/2}$) and 463.6 eV (Ti^{4+} $2p_{1/2}$). The addition of single dopants in the guise of Dy-SD (Figure 4B), Y-SD (Figure 4C), Ca-SD (Figure 4D), Gd-SD (Figure 4E), and Dy(N)-SD (Figure 4F) in all cases resulted in not only the preservation of Ti^{4+} (red) but also the formation of Ti^{3+} (purple) (Table S4). As such, the red line denotes the Ti^{4+} $2p_{3/2}$ peak, whereas the purple line can be ascribed to the Ti^{3+} $2p_{3/2}$ signal. Previously, it has been shown that the presence of Ti^{3+} species was suggestive of an increase in conductivity and a concomitant enhancement in electrochemical performance.[4,13]

Doped Samples: We observed a shift in the Ti^{3+} and Ti^{4+} peaks toward higher energies for both the Ca-SD and Gd-SD samples as compared with their undoped counterparts. This trend in behavior was previously observed not only for Ca-doped LTO[13] but also for analogous Gd-doped LTO samples.[21] The observed shift within the Ca-SD material most likely derives from an increase in electronegativity arising from the substitution of Ca for Li, a scenario which would lead to a slight increase in the electron density surrounding Ca with a corresponding loss around Ti.
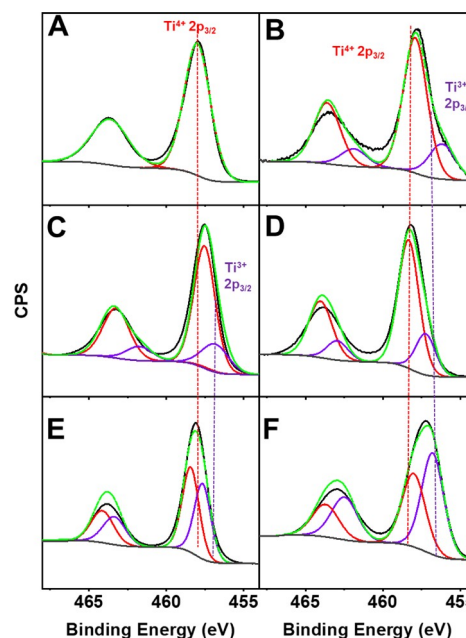

Figure 4. Ti 2p region of not only (A) pure LTO but also the series of singly-doped samples of (B) Dy-SD, (C) Y-SD, (D) Ca-SD, (E) Gd-SD, and (F) Dy(N)-SD.

We envision a similar explanation accounting for the shift toward higher energies for the Ti peaks, associated with Gd-SD. In that system, Gd can presumably co-dope onto the Li site as well, since it maintains a higher electronegativity value (1.2) as compared with that for Li (0.98), implying a similar electron density shift toward Gd and away from Ti.[19] It should be noted that data on the Gd-SD sample are complicated by a possible Gd_2O_3 impurity, although the presence of this metal
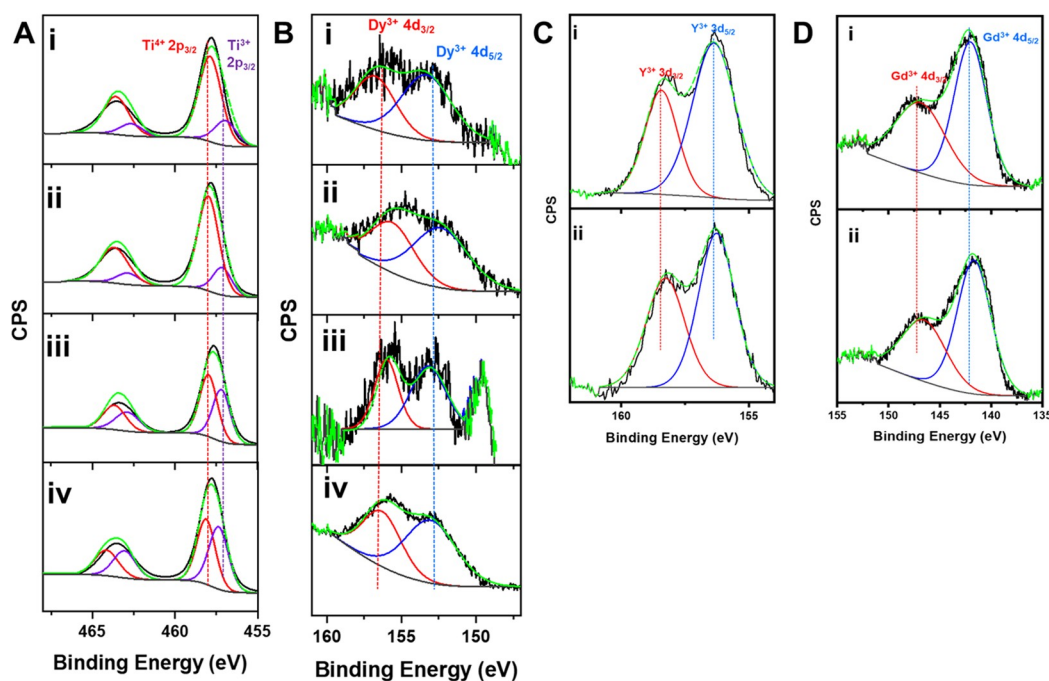
Figure 5. (A) Ti 2p region of the triply-doped samples: (i) Dy-TD, (ii) Y-TD, (iii) Gd-TD, and (iv) Dy(N)-TD. (B) Dy 4d region for (i) Dy-SD, (ii) Dy(N)-SD, (iii) Dy-TD, and (iv) Dy(N)-TD. (C) Y 3d region for (i) Y-SD and (ii) Y-TD. (D) Gd 4d region for (i) Gd-SD and (ii) Gd-TD.

oxide was not obviously apparent from our XRD data, implying that Gd may be co-doping at the Li site.[13] Interestingly, we detected no perceptible shift in the Ti peak positions between pure LTO and either the Dy-SD or Dy(N)-SD samples. By contrast, with the Y-SD sample, we found a shift toward lower energies within the Y-SD sample, a finding consistent with what has been previously reported in the literature for Y-doped LTO materials.[23]

The Ti 2p region was also investigated for the series of triply-doped samples (Figure 5A, Table S4). As observed in Table 1, all four of the triply-doped samples, namely, Dy-TD

Table 1. Ratio of Ti^{4+} to Ti^{3+}, as Computed from XPS Data, Associated with the Ti 2p Region

sample	Ti^{4+} 2p$_{3/2}$	Ti^{3+} 2p$_{3/2}$
pure LTO	1.0	0
Dy-SD	4.6	1.0
Y-SD	3.5	1.0
Ca-SD	4.0	1.0
Gd-SD	1.1	1.0
Dy(N)-SD	0.8	1.0
Cl-SD	3.3	1.0
Dy-TD	3.5	1.0
Y-TD	4.0	1.0
Gd-TD	1.2	1.0
Dy(N)-TD	1.0	1.0

(Figure 5Ai), Y-TD (Figure 5Aii), Gd-TD (Figure 5Aiii), and Dy(N)-TD (Figure 5Aiv) yielded both Ti^{4+} and Ti^{3+} peaks as well, a finding consistent with an increased electronic conductivity as compared with the pure LTO sample alone. There was very little change in the peak values for the analyzed materials. The exception was Gd-TD in which the trend for the peak positions of both Ti^{4+} and Ti^{3+} peaks behaved similarly with its Gd-SD and Ca-SD counterparts.

As such, the amount of Ti^{3+} was carefully evaluated in order to compare behavior across the range of materials analyzed. To quantitatively assess the concentrations of Ti^{3+} within all of these samples, the Ti^{4+}:Ti^{3+} ratio was computed (Table 1).[4,24,25] With respect to the initial set of lanthanide-based singly-doped samples, it was observed that Dy(N)-SD yielded the highest amount of Ti^{3+} with a Ti^{4+}:Ti^{3+} ratio of 0.8:1. With the other samples, the measured Ti^{4+}:Ti^{3+} ratios were noted to be 1.1:1, 3.5:1, and 4.6:1 for Gd-SD, Y-SD, and Dy-SD, respectively. Though one would have expected that samples possessing the highest amount of Ti^{3+} species would generate the greatest levels of conductivity, this simplistic picture is complicated by the fact that excessive doping can potentially lead to structural strain and hence, an overall decrease in performance as an LIB anode.

Furthermore, with respect to the triply-doped samples, similar types of behavior were observed. The highest Ti^{3+} content was noted in the Ti^{4+}:Ti^{3+} ratio of 1:1 for the Dy(N)-TD sample. The corresponding Ti^{4+}:Ti^{3+} ratios for Gd-TD, Dy-TD, and then finally Y-TD were computed to be 1.2:1, 3.5:1, and 4:1, respectively. The data highlight the following observations. (1) In both the singly-doped and triply-doped samples, LTO containing either Gd or Dy(N) yielded the highest Ti^{4+}:Ti^{3+} ratios. (2) Within these samples in terms of increasing Ti^{3+} content, the trend was Gd-TD < Gd-SD < Dy(N)-TD < Dy(N)-SD with the implication that in general, the singly-doped samples gave rise to higher Ti^{3+} concentrations as compared with their triply-doped counterparts. The key exception to this trend resided in the Dy-SD / Dy-TD series. The amount of Ti^{3+} content appeared to drop even more precipitously in progressing from the singly to triply-doped analogues of Y (Table 1).

3.1.3.2. Analysis of the N 1s Region. To account for the notably large increase in Ti^{3+} concentration upon progressing from Dy-SD to Dy(N)-SD and in parallel, Dy-TD to Dy(N)-TD, the extent of doping of the halide anion was evaluated for

the relevant Dy salt precursor used. Specifically, we accounted for the amount of incorporated (i) Cl within Dy-SD and by analogy, (ii) N within Dy(N)-SD. To do so, we probed the Cl 2p region for Dy-SD in addition to the N 1s region for Dy(N)-SD and Dy(N)-TD samples to determine if the counterion of the associated dysprosium salt had actually been incorporated within the as-prepared material (Figure S2 and Table S4). From initial results, it was observed that when the Dy chloride salt was used, no chloride was apparently detected within the resulting material (Figure S2A). Conversely, when the Dy nitrate salt was utilized, a peak ascribable to N 1s was located at 398.3 eV (Figure S2B) for Dy(N)-SD and at 399.1 eV (Figure S2C) for Dy(N)-TD (Table S4). This finding has previously been attributed to the formation of O−Ti−N linkages, indicative of successful doping of nitrogen originating from the nitrate.[26]

Furthermore, the addition of the N doping plays a significant role in the increase in Ti^{3+} content. Specifically, both singly and triply-doped samples derived from Dy nitrate maintain significantly higher Ti^{3+} amounts as compared with analogous Dy-SD and Dy-TD materials. The peak shift observed for N 1s could be correlated with the changes in Ti^{3+} concentration. As an example, because Dy(N)-SD yielded more Ti^{3+} species as compared with Dy(N)-TD, the corresponding position of its measured N 1s binding energy was more noticeably shifted by as much as 0.8 eV. Nevertheless, it should be noted that the effect of varying the overall concentration of N is almost negligible; there is only a very small change in the N atomic % (1.3 to 1.6) upon formation of a triply-doped material (Table S6). This observation would indicate that whereas the presence of N doping is significant in and of itself, the actual concentration of N does not necessarily impact upon the Ti^{3+} concentration in a direct and linearly proportionate manner.

3.1.3.3. Analysis of the Dy 4d Region. The lanthanide ion series was subsequently evaluated (Figure 5B−D). As an initial example, the Dy 4d region was investigated in Figure 5B. Specifically, Dy^{3+} peaks were noted not only at 153.1 and 156.4 eV for Dy-SD (Figure 5Bi) but also at 152.2 and 155.4 eV for Dy(N)-SD (Figure 5Bii). This pair of signals could be ascribed to the $4d_{5/2}$ and $4d_{3/2}$ peaks, respectively, wherein the Dy(N)-SD sample yielded a slight negative shift toward lower energies as compared with its chloride salt counterpart, most likely due to the incorporation of nitrogen.

With respect to their triply-doped analogues, there was also successful Dy doping in both samples with observed peaks ascribed to Dy^{3+} $4d_{5/2}$ (Dy-TD: 153.2 eV, Dy(N)-TD: 152.9 eV) in addition to Dy^{3+} $4d_{3/2}$ (Dy-TD: 156.0 eV, Dy(N)-TD: 156.3 eV) (Figure 5Biii,iv, Table S4). By analogy with singly-doped samples, a slight negative shift toward lower energies was observed in progressing from the Dy-TD to the Dy(N)-TD samples. Nevertheless, with Dy, we emphasize that both samples incorporating either single dopants or their associated triply-doped counterparts demonstrated successful dopant ion incorporation (Table S4).

The dopant concentration within each as-prepared sample was quantitatively computed. As a general comment, what matters most in this analysis are not necessarily the absolute values we have calculated herein but rather the relative, comparative trends detected across different series of samples. For example, for a singly-doped lanthanide-based sample, the amount of lanthanides (Ln) was estimated by dividing the Ln area analyzed by the sum of the relative areas of Ln and Ti

(Table S6, Formula S2).[24,27] Both samples singly doped with Dy yielded similar measured amounts of this lanthanide, i.e., 0.7% (Dy-SD) and 0.6% (Dy(N)-SD), respectively. Furthermore, in the case of Dy-SD versus Dy-TD using the chloride precursor, we found a decrease in Dy atomic % from 0.7% within Dy-SD to 0.2% within Dy-TD (Table S6). Conversely, in the case of Dy(N) using the nitrate precursor, in progressing from singly-doped to triply-doped samples, there was a calculated increase in the Dy atomic % from 0.6% to 1.3% (Table S6).

While the apparent increase in dopant incorporation within triply-doped samples emanating from the use of nitrate (1.3%) versus chloride (0.2%) precursors may have resulted from nuanced differences in anion solubility, dispersibility, and/or size, a more likely scenario is that use of the nitrate precursor promoted a comparatively greater surface localization or enrichment of Dy as opposed to any "true" increase in overall Dy incorporation. That is, the use of nitrates may have simply altered the spatial distribution of Dy to favor the outer surface, to which XPS is intrinsically more sensitive in detecting. Support for this hypothesis resides in the fact that whereas there were ostensible changes in Dy content within the triply-doped materials, there were far less meaningful fluctuations in Ti^{3+} concentration across this series. Overall, these data, implying the lack of a direct, linear correlation between relative Dy and Ti^{3+} amounts, suggest that there may be an upper "threshold" limit as to exactly how much Dy can effectively co-exist with the other dopants present within these materials, i.e., namely Cl and N at the O sites and Ca at the Li sites.

3.1.3.4. Analysis of the Y 3d Region. With respect to Y, the series of Y-doped materials also evinced a strong signal associated with Y^{3+}. In particular, the 3d region gave rise to pairs of Y^{3+} $3d_{5/2}$ and Y^{3+} $3d_{3/2}$ peaks that could be localized at 156.2 eV ($3d_{5/2}$, blue) and 158.2 eV ($3d_{3/2}$, red) for Y-SD (Figure 5Ci) in addition to 156.4 and 158.4 eV for Y-TD (Figure 5Cii; Table S4), respectively. In this case, there was no apparent difference in peak position in progressing from the singly-doped to the triply-doped samples. However, the dopant concentration was impacted. Specifically, the atomic % of Y rose from 1 to 1.9% with regards to the singly- and triply-doped samples, respectively. By analogy with Dy, because we were using Y nitrate precursors, this observation could be plausibly ascribed to preferential surface enrichment of Y atoms as opposed to any actual changes in the concentration of Y (Table S6). Moreover, as with Dy, this finding supports the idea that the Y dopant amount does not necessarily directly correlate with the amount of Ti^{3+} generated.

3.1.3.5. Analysis of the Gd 4d Region. Regarding Gd, evidence for successful doping arises from the appearance of strong signals associated with Gd^{3+} 4d peaks at 142.0 and 146.9 eV, denoted as $4d_{5/2}$ (blue) and $4d_{3/2}$ (red), respectively (Table S4, Figure 5Di) for the Gd-SD sample in addition to those located at 141.7 eV (Gd^{3+} $4d_{5/2}$) and 146.5 eV (Gd^{3+} $4d_{3/2}$) for the Gd-TD material. The slight shift toward lower energies for the triply-doped versus the singly-doped samples provides an indication that the other dopants such as Ca and Cl are likely present as well within Gd-TD (Figure 5Dii; Table S4). Interestingly, we noted that there appeared to be a slight increase in Gd content in the analysis of the triply-doped (2.5%) versus the singly-doped (2.0%) sample, which is opposite in behavior to that of the corresponding Ti^{3+} content, reinforcing the concept that the Gd and Ti^{3+} dopant levels do
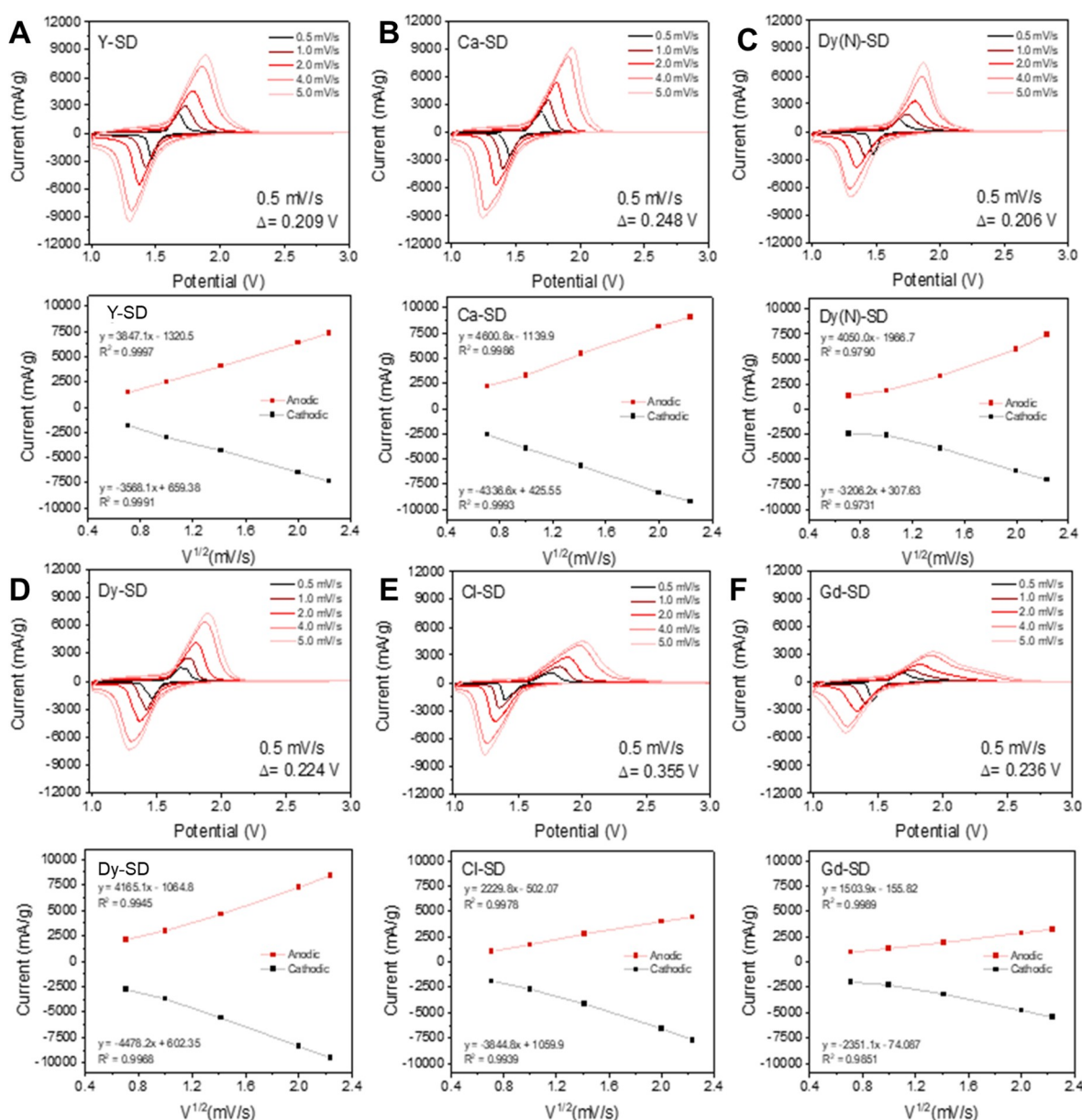
Figure 6. Cyclic voltammograms and respective peak current versus the square root of scan rate plots for singly-doped LTO (A) Y-SD, (B) Ca-SD, (C) Dy(N)-SD, (D) Dy-SD, (E) Cl-SD, and (F) Gd-SD samples.

not necessarily track with each other, presumably due to the complicating co-presence of other dopants (Table S6).

3.1.3.6. Analysis of Ca 2p Region and Cl 2p Region. With respect to Ca, for the Ca-SD sample, the Ca 2p region (Figure S3A) was indicative of successful doping into the LTO matrix with the appearance of Ca^{2+} 2p peaks located at 346.8 and 350.3 eV, associated with the $2p_{3/2}$ (red) and $2p_{1/2}$ (blue) peaks, respectively (Table S4). Furthermore, we observed a negative shift to lower energies upon formation of all 4 triply-doped samples, i.e., Dy-TD (Figure S2B), Y-TD (Figure S2C), Gd-TD (Figure S2D), and Dy(N)-TD (Figure S2E). This result can most likely be ascribed to the concomitant presence of the co-doped, electron-rich lanthanide ions, which would have the consequential effect of enhancing the local electron density and perceptibly raising Ti^{3+} concentration within the sample environment. The exception to this trend, i.e., Y-TD, maintained approximately the same $Ti^{4+}:Ti^{3+}$ ratio as that of Ca-SD. Furthermore, this behavior correlates with the parallel

increase in energy in the Li 1s peak in advancing from Ca-SD (54.1 eV) onward to Dy-TD (54.0 eV), Y-TD (53.8 eV), and ultimately Dy(N)-TD (53.9 eV) (Figure S5). These data are consistent with a corresponding transfer of electron density away from Li (i.e., positive shift in eV) to Ca (i.e., negative shift in eV) upon incorporation of the lanthanides and their associated Cl and nitrate anions. The exception to this trend, i.e., Gd-TD (54.3 eV), exhibited a shift to higher energy, which can most likely be explained by direct competition with Gd and hence, displacement of Ca with Gd at the Li sites because of Gd's higher electronegativity value (i.e., 1.2) as compared with that of Ca (i.e., 1.0).

The amount of Ca at the Li sites appeared to have significantly decreased by as much as 10-fold within all of the triply-doped samples (Table S6). Among the various triply-doped samples, the amount of Ca appeared to be the highest within the Gd-TD and Dy(N)-TD samples, yielding 4.4 and 4.5% quantities, respectively (Table S6). Nevertheless, these
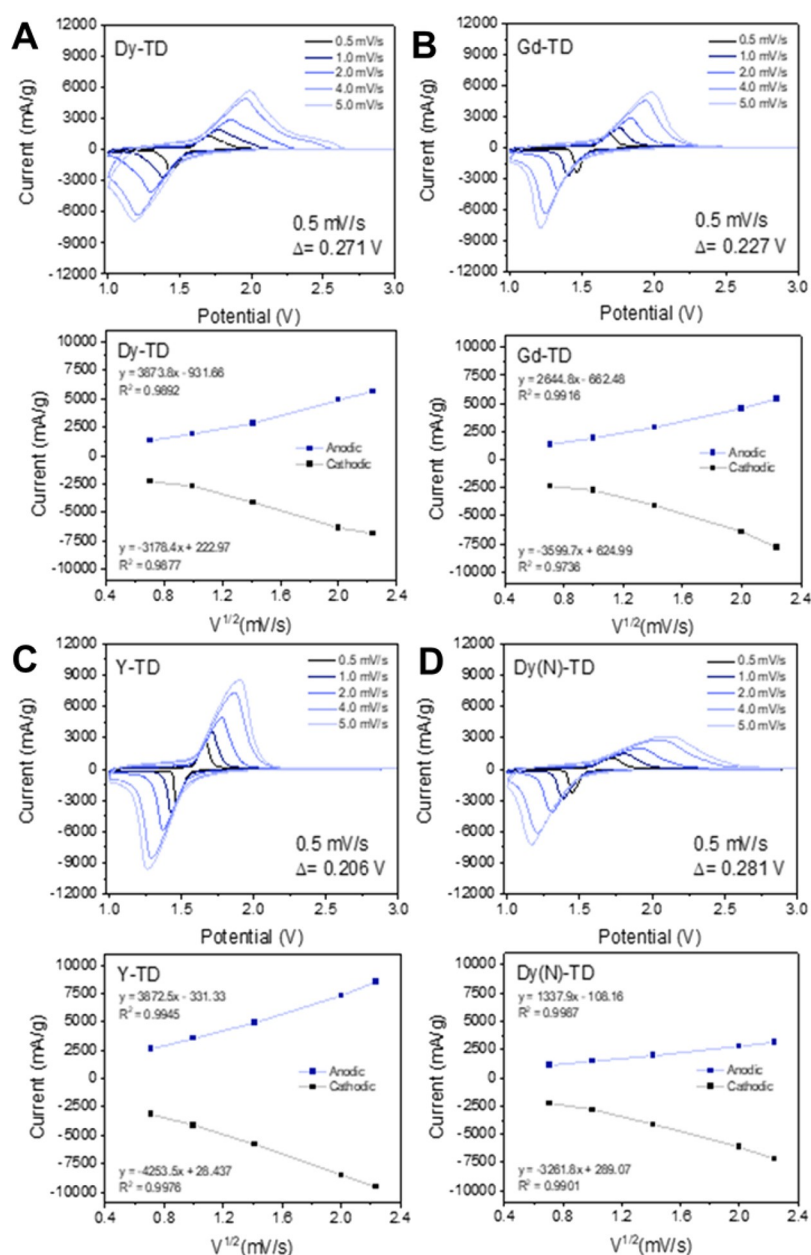
Figure 7. Cyclic voltammograms and respective peak current versus the square root of scan rate plots for triply-doped LTO (A) Dy-TD, (B) Gd-TD, (C) Y-TD, and (D) Dy(N)-TD materials.

values were much smaller than what were noted for the Ca-SD material (23.2%). In addition, a decrease in the amount of Ca doping observed in Dy-TD versus Dy(N)-TD implies that the identity of the halide counter-anion remains an important variable, perhaps due to the preferential surface localization of Dy and Ca ions induced by the presence of the nitrate.

The Cl-SD sample was systematically characterized in a previous paper.[4] Remarkably, our data show that the chloride dopant concentrations remain relatively constant across the entire range of triply-doped samples tested, regardless of the lanthanides involved (Figure S5, Table S4 and S6).

Finally, the relative surface composition of Ca was calculated (Table S7, Formula S3) to verify that the presence and degree of incorporation of the dopant with respect to the underlying LTO stoichiometry.[28] To account for Ca content within Ca-SD, we summed up the relative areas of Ca and Li to capture the possible sites for Ca localization and divided that by the

sum of the relative areas of all of the other components (i.e., Ca, Li, O, and Ti). In general, it was observed that all of the singly doped samples retained the inherent 4 Li:5 Ti:12 O ratio.

3.1.3.7. Summary. XPS analysis was consistent with the idea that doped materials, specifically Dy(N)-SD, Dy(N)-TD, Gd-SD, and Gd-TD, may exhibit an increase in conductivity (especially as compared with the other lanthanide systems tested herein) due to the presence of high amounts of Ti^{3+}. Furthermore, our data also suggest that Dy(N) materials possess a greater Ti^{3+} content and hence, an enhanced conductivity as compared with analogous doped samples, prepared using Dy chloride precursors. Additionally, our XPS evidence implies that Gd may potentially co-dope into both the Li and the Ti sites. CV analysis was subsequently used as a complementary tool with which to evaluate the diffusion
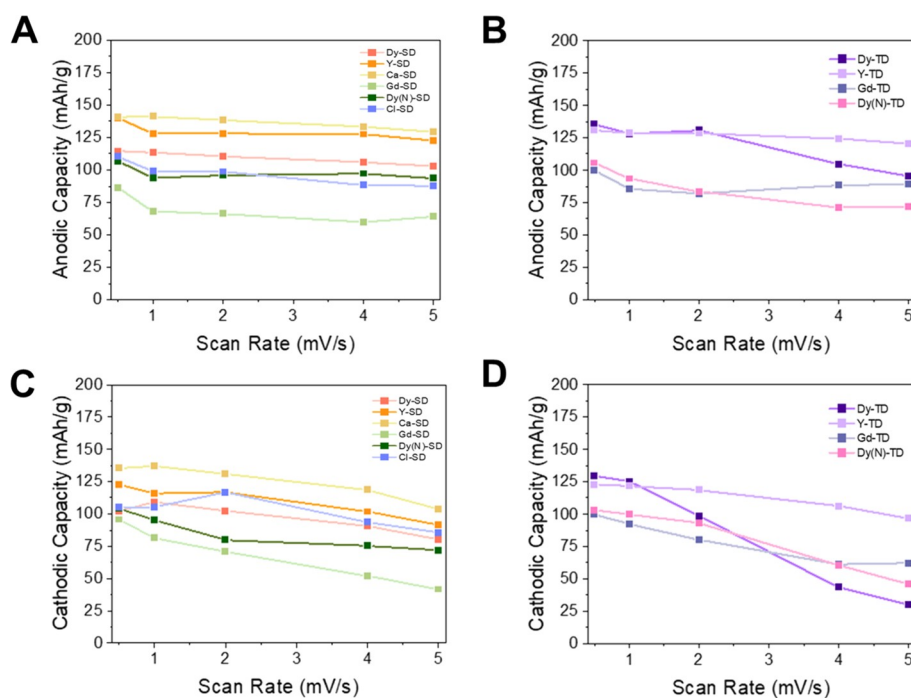
Figure 8. Capacities calculated from the integration of the (A,B) anodic and (C,D) cathodic peaks throughout each scan rate for (A,C) singly-doped and (B,D) triply-doped materials.

properties of these doped materials for their possible use as LIB anodes.

3.2. Cyclic Voltammetry Analysis

That is, to investigate the diffusion properties of the material, cyclic voltammetry (CV) data of pristine LTO, Y-SD, six singly-doped LTO (Dy-SD, Ca-SD, Gd-SD, Cl-SD, and Cl-SD), and five multiply-doped LTO samples (Dy(N)-SD, Y-TD, Dy-TD, Gd-TD, and Dy(N)-TD) were collected using scan rates of 0.5, 1.0, 2.0, 4.0, and 5.0 mV s^{-1} (Figures 6 and 7, Figure S6, and Table S8). CV was selected as the analysis mode with which to assess the relative reversibility of the electrochemistry through examination of the ΔE_{peak} values. Furthermore, the slope of the peak current (I_p) versus the square root of the scan rate was determined for the oxidation and reduction of each material to evaluate diffusion control for these electrochemical processes (Tables S9–S13).[29]

The ΔE_{peak} values were determined for each material sample as a function of scan rate (Table S8), thereby allowing for an estimate of redox reversibility for each system. In general, using pure LTO as a baseline (0.286 V at 0.5 mV/s, 0.768 V at 5.0 mV/s), most systems showed either similar or smaller ΔE_{peak} values with the exception of three samples, namely, Cl-SD (0.355 V at 0.5 mV/s, 0.766 V at 5.0 mV/s), Dy-TD (0.271 V at 0.5 mV/s, 0.808 V at 5.0 mV/s), and Dy(N)-TD (0.281 V at 0.5 mV/s, 0.936 V at 5.0 mV/s). Hence, relative to the pure LTO sample, it may be possible to compare the effect of doping upon Li$^+$ diffusivity and reaction kinetics on the spinel structure in general. Previous literature reports have proposed that controlling the crystallite size and subsequent lattice parameters offer a viable means with which to shorten the Li$^+$ transfer pathway and thereby improve upon effective diffusivity.[17,30] To a reasonable first-order approximation, in this study, the crystallite sizes among all of the samples (Table S2) are relatively similar in magnitude. Therefore, any measurable electrochemical differences can most likely be

ascribed to the chemical nature of the incorporated dopants themselves and to accompanying changes in the ionic sites in which they reside within the overall structure.

3.2.1. Singly-Doped Systems.
The various singly-doped materials were analyzed using the linear fit for the peak currents vs scan rate plots (Figure 6). In particular, the Dy(N)-SD, Dy-SD, Y-SD, Gd-SD, and Ca-SD samples all exhibited lower ΔE_{peak} values as compared with pure LTO (Figure S6) across the scan rates tested, indicative of enhanced diffusivity for these doped materials. Furthermore, we highlight that Dy(N)-SD and Y-SD evinced the lowest overall ΔE_{peak} values detected, which was a slightly unexpected observation given that the Y-SD material maintained a relatively low Ti^{3+} concentration, as per our prior XPS analysis. Hence, we postulate that the despite the expected increase in conductivity due to the greater incorporation of Ti^{3+} content, this particular parameter is not necessarily the sole determinant or arbiter of efficient Li ion diffusivity.

By contrast, Gd-SD yielded the highest ΔE_{peak} readings as compared with the other singly-doped lanthanides, suggestive of comparatively poorer diffusivity within this system (Table S8). In this case, this observation does correlate with the above XPS analysis and can most likely be attributed to co-doping of Gd at both the Li and Ti sites. As we have previously implied, excess doping, i.e., above a certain element-specific threshold, can lead to poor kinetics due to a high volume strain on LTO, as has been previously observed with prior lanthanide doped-LTO samples reported in the literature.[17]

With respect to the Cl-SD sample, this material evinced an increase in ΔE_{peak} as compared with the pure LTO material, consistent with a decreased Li ion mobility as compared with the pristine sample. One possible explanation is that the Cl$^-$ ion replaces anionic O^{2-} content within the pristine structure, a scenario which can negatively impact upon the effectiveness of Li$^+$ diffusion pathways. Not surprisingly, all of these findings would lead to the relatively less favorable potential of using Cl
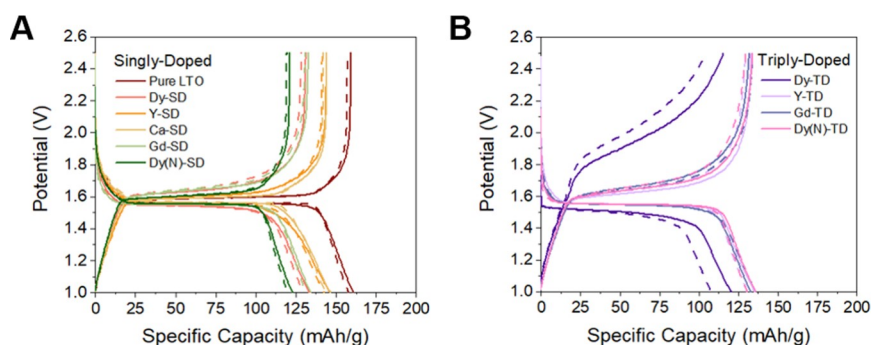
Figure 9. Galvanostatic cycling of (A) pure LTO, singly-doped, and (B) triply-doped materials, measured at 0.2 C at cycle 5 (solid line) and cycle 20 (dashed line).

as a single dopant, by comparison with the other dopants tested herein. By contrast, the Ca-SD sample gave rise to a lower ΔE_{peak} reading as compared with pure LTO, suggestive of a more favorable ion mobility. When comparing Cl-SD and Ca-SD samples, our data indicate that doping at the Li site, as opposed to the O site, appears to yield a greater impact on the resulting ion mobility.

3.2.2. Triply-Doped Systems. Notably, "triple doping" has not been previously studied, and the effects of triply replacing the ions within LTO were analyzed in the same manner. Both the Y-TD and Gd-TD materials (Figure 7, Table S8) yielded lower ΔE_{peak} values than pure LTO alone, consistent with the presence of enhanced diffusivity and favorable Li mobility for these systems. However, whereas Y-TD gave rise to a lower ΔE_{peak} value lower than its SD counterpart, the exact opposite was true for Gd. Therefore, we hypothesize that in the Gd-TD sample, the combination of the co-doping of the Gd ion into both the Li and the Ti sites, coupled with the complicating presence of additional Ca^{2+} and Cl^- doping, led to an overall structural instability of this material.

Similar to Gd, the Dy-TD and Dy(N)-TD samples likewise gave rise to higher ΔE_{peak} values than their SD counterparts; in fact, these were greater in magnitude than those observed with pure LTO overall. When comparing Dy-TD and Dy(N)-TD, Dy(N)-TD generated greater ΔE_{peak} values than Dy-TD, which we had previously attributed to an increased strain on the LTO structure upon increasing dopant concentrations. Therefore, according to the overall CV analysis, the optimized samples demonstrating increased ion mobility comprised Y-SD, Y-TD, and Dy(N)-SD, all of which displayed significantly lower ΔE_{peak} values as compared with the pure LTO control.

3.2.3. Additional Analysis. The areas under the anodic and cathodic peaks provided in Figures 6 and 7 were integrated to assess capacity achieved by each sample as a function of scan rate in order to provide an idea of the nature of the various materials' stability (Figure 8). The scan rate dependence is an indication of the rate capability for each material and is suggestive of trends in effective lithium-ion diffusion. In general, the capacity value appeared to be the highest at the lowest scan rate of 0.5 mV/s and the lowest at the highest scan rate of 5 mV/s.

Regarding the anodic capacity of singly-doped materials (Figure 8A), the material possessing arguably the highest anodic capacity and stability was the Ca-SD material followed closely by Y-SD (Figure 8A). Notably, the capacity delivered was fairly constant over all of the scan rates accessed for the Ca-SD and Dy-SD samples. The other samples showed a

relatively small decrease in capacity between the 0.5 and 2.0 mV/s scan rates. Similarly, the anodic capacities of the triply-doped materials (Figure 8B) also revealed relatively stable capacities as a function of scan rate. The one notable exception was the Y-TD sample, characterized by a relatively steady capacity at all scan rates, which ended up being the highest value measured among all of the TD samples tested at scan rates of 4 and 5 mV/s.

By contrast, the cathodic capacity of the singly doped materials showed a greater dependence on scan rate. Specifically with the exception of the Cl-SD material (Figure 8C), the singly-doped samples evinced a generally decreasing trend in capacity with increasing scan rate. The cathodic capacity for the TD samples (Figure 8D) also demonstrated a scan rate dependence, wherein the delivered capacity decreased with increasing scan rate. The Y-TD sample yielded the least rate dependence based on scan rate, whereas the Dy-TD sample was indicative of the highest correlation with scan rate.

3.2.4. CV Summary. The Ca-SD, Y-SD, Y-TD, and Dy(N)-SD samples evinced promising Li ion diffusion and reversibility for the electrochemical reactions occurring within the LTO system. Collectively, these data likely indicate that doping at the Li site coincides with a more noticeable effect upon the electrochemical performance as compared with doping at either the O or Ti sites. Moreover, there is no firm and direct correlation between Ti^{3+} content (deduced from XPS analysis) and ion mobility/diffusivity, although greater Ti^{3+} concentrations are conducive to increased conductivity. Furthermore, strain issues associated with the presence of excess dopant may have a perceptible impact on structural stability and the corresponding ion mobility. While these themes have been previously discussed with singly-doped materials, to the best of our knowledge, this is the first time in which similar trends have been assessed and demonstrated within triply-doped systems for LIB anodes. In general, as a result of the doping process, these samples have the potential for giving rise to relatively high capacities and favorable Coulombic efficiencies with increased scan rates.

The galvanostatic cycling of not only LTO but also their singly and triply-doped analogues was investigated with the data presented in Figure 9. The singly doped samples all showed only minor changes between the 5th and 20th cycles. Specifically, the singly-doped materials, namely, Y-SD (Figure 9A, orange) and Ca-SD (Figure 9A, yellow), delivered the highest capacity at 133 and 144 mAh/g, respectively, in agreement with the trend observed in the CV data. The reversibility of the samples suggests that the enhanced doping

ability and the higher induced ion mobility herein can collectively assist in maintaining the pristine structure of the LTO host material, even after repeated cycling steps, as evinced by the retention of the voltage profiles. By contrast, the Dy(N)-SD sample delivered the lowest capacity measured of 120 mAh/g at the end of 20 cycles. Nonetheless, regardless of the capacity achieved, all of the singly-doped materials maintained similar voltage profiles to that of the pure material. Specifically, these profiles were characterized by the presence of a plateau at ~1.56 V during the discharge process, coupled with the appearance of a reversible plateau at ~1.60 V during charging. By means of comparison, after 20 cycles, the pure sample attained a value of 158 mAh/g upon lithiation.

Interestingly, the Y-TD, Gd-TD, and Dy(N)-TD samples all performed similarly (~130−135 mAh/g after the 20th lithiation), regardless of the lanthanide dopant substituted into the LTO host material. Moreover, the singly-doped samples gave rise to the same voltage profile as that of their triply-doped counterparts. The one outlier in this series was Dy-TD, wherein the discharge voltage plateau appeared at a lower voltage of 1.53 V and began to level out upon charging at ~1.80 V. These findings highlighted the presence of irreversibility, and hence, not surprisingly, we noted a correspondingly lower capacity after 20 cycles (108 mAh/g) for this sample. In effect, the presence of increased dopants within the Dy-TD sample (unlike for the analogous Dy(N)-TD material) may have negatively impacted its measured electrochemical performance throughout the cycling process.

Collective consideration of these galvanostatic data coupled with the complementary CV analysis along with the capacities calculated by the integration of anodic and cathodic peaks indicated that samples incorporating not only doping of Ca into the Li site but also doping of Y into the Ti site yielded the highest cycling ability. Furthermore, as a function of scan rate dependence in the CV, the Dy-TD sample exhibited the greatest amount of capacity reduction, noted among both sets of singly- and triply-doped samples, a finding which is consistent with the highest capacity decrease we measured as a consequence of the galvanostatic cycling process.

4. CONCLUSIONS

To summarize, individual elements associated with Ca, Dy, Gd, Y, and Cl could be successfully singly and discretely doped into LTO without necessarily degrading either the morphology or the chemical composition, as can be concluded from a collective consideration of SEM, XPS, HRTEM-EDS, and XRD data. A similar set of conclusions could be derived for the 4 sets of triply-doped samples synthesized for the first time by a previously developed facile hydrothermal method, in which Ca (or Gd) favored the Li site, Ln (Dy, Y, or Gd) localized at the Ti site, and Cl was substituted at the O site, respectively. The resulting samples exhibited and retained the original micron-scale flower-like morphology from SEM with the expected chemical compositions confirmed by XRD. Moreover, our HRTEM-EDS results were consistent with a reasonably homogeneous dispersion of elements throughout all of the as-prepared samples.

The surface chemistry of these materials was investigated using XPS, which suggests successful substitutional doping involving Ca, Dy, Y, Gd, and Cl. Furthermore, from an evaluation of changes in the Ca 2p and Li 1s regions, Gd may potentially contribute to doping not only at the Ti site but also at the Li site, whereas Dy and Y doping predominantly occurs

only at the Ti sites. The choice of metal counterion that is used to synthesize these materials also is crucial in that the use of a precursor nitrate as opposed to a chloride anion favors not only higher overall lanthanide dopant incorporation and surface localization but also enhancements in the amount of N doping, presumably due to the increased amounts of Ti^{3+} content within the system. With the complementary CV and cycling analyses, it was shown that (i) with the Ca-doped samples, doping at the Li site, as opposed to the O site, appeared to yield a greater impact on the resulting ion mobility, (ii) the Y-doped series, associated with doping at the Ti^{4+} site, evinced an enhanced cycling stability as compared with the other lanthanides, and (iii) Dy(N)-SD samples possessed the highest amount of Ti^{3+} species not only indicative of favorable conductivity but also conducive to reasonable Li ion diffusion.

In conclusion, in our study, both triply-doped and singly-doped LTO materials were carefully evaluated as potential candidates as anodic LIB materials due to their potential for relatively increased mobility, Li ion diffusivity, capacity, and stability. In particular, the ability to dope LTO with three different elemental species allowed us to probe issues, such as the effects of varying the dopant chemistry and identity upon the observed electrochemical performance. Specifically, as compared with singly doping LTO, the use of multiple distinctive types of dopants likely improved the overall conductivity of this material by increasing the concentration of Ti^{3+} species and thereby enhancing Li ion diffusivity in a synergistic manner. The expectation was that since the ions were all doping into dissimilar sites, in principle, we could independently adjust and accordingly correlate the individual amounts of these three different dopants that would end up spatially localizing at the Li, Ti, and O sites, with the measured electrochemical behavior. Hence, additional studies will aim at precisely controlling the actual amounts (over a broader concentration range) of these singular Ca, lanthanide, and chloride dopant ions in order to tune the measured Ti^{3+} content within the system so as to achieve the overall goal of optimizing the entire doping process.

■ ASSOCIATED CONTENT

ⓢ Supporting Information

The Supporting Information is available free of charge at https://pubs.acs.org/doi/10.1021/acsphyschemau.1c00044.

> Microscopy and spectroscopy characterization of pristine LTO; XPS of Cl 2p, Ca 2p, Li 1s, and N 1s regions; CVs of pure LTO; relevant equations for XPS analysis; tables of previous electrochemical studies on doped LTO materials; tables related to XRD and XPS analysis of LTO; and tables corresponding to CV analysis on doped LTO systems (PDF)

■ AUTHOR INFORMATION

Corresponding Author

Stanislaus S. Wong − *Department of Chemistry, State University of New York at Stony Brook, Stony Brook, New York 11794-3400, United States;* ⓞ orcid.org/0000-0001-7351-0739; Email: stanislaus.wong@stonybrook.edu

Authors

Kenna L. Salvatore − *Department of Chemistry, State University of New York at Stony Brook, Stony Brook, New York 11794-3400, United States*

Mallory N. Vila − *Department of Chemistry, State University of New York at Stony Brook, Stony Brook, New York 11794-3400, United States; Institute for Electrochemically Stored Energy, State University of New York at Stony Brook, Stony Brook, New York 11794, United States;* orcid.org/0000-0002-8745-1159

Genesis Renderos − *Department of Chemistry, State University of New York at Stony Brook, Stony Brook, New York 11794-3400, United States; Institute for Electrochemically Stored Energy, State University of New York at Stony Brook, Stony Brook, New York 11794, United States*

Wenzao Li − *Department of Chemistry, State University of New York at Stony Brook, Stony Brook, New York 11794-3400, United States; Institute for Electrochemically Stored Energy, State University of New York at Stony Brook, Stony Brook, New York 11794, United States;* orcid.org/0000-0003-3098-6870

Lisa M. Housel − *Institute for Electrochemically Stored Energy, State University of New York at Stony Brook, Stony Brook, New York 11794, United States; Interdisciplinary Science Department, Brookhaven National Laboratory, Upton, New York 11973, United States;* orcid.org/0000-0001-8429-5480

Xiao Tong − *Center for Functional Nanomaterials, Brookhaven National Laboratory, Upton, New York 11973, United States; Department of Materials Science and Chemical Engineering, State University of New York at Stony Brook, Stony Brook, New York 11794-2275, United States*

Scott C. McGuire − *Department of Chemistry, State University of New York at Stony Brook, Stony Brook, New York 11794-3400, United States*

Joceline Gan − *Department of Chemistry, State University of New York at Stony Brook, Stony Brook, New York 11794-3400, United States*

Ariadna Paltis − *Department of Chemistry, State University of New York at Stony Brook, Stony Brook, New York 11794-3400, United States*

Katherine Lee − *Department of Chemistry, State University of New York at Stony Brook, Stony Brook, New York 11794-3400, United States*

Kenneth J. Takeuchi − *Department of Chemistry, State University of New York at Stony Brook, Stony Brook, New York 11794-3400, United States; Institute for Electrochemically Stored Energy, State University of New York at Stony Brook, Stony Brook, New York 11794, United States; Interdisciplinary Science Department, Brookhaven National Laboratory, Upton, New York 11973, United States;* orcid.org/0000-0001-8129-444X

Amy C. Marschilok − *Department of Chemistry, State University of New York at Stony Brook, Stony Brook, New York 11794-3400, United States; Institute for Electrochemically Stored Energy, State University of New York at Stony Brook, Stony Brook, New York 11794, United States; Interdisciplinary Science Department, Brookhaven National Laboratory, Upton, New York 11973, United States;* orcid.org/0000-0001-9174-0474

Esther S. Takeuchi − *Department of Chemistry, State University of New York at Stony Brook, Stony Brook, New York 11794-3400, United States; Institute for Electrochemically Stored Energy, State University of New York at Stony Brook, Stony Brook, New York 11794, United States; Interdisciplinary Science Department, Brookhaven National Laboratory, Upton, New York 11973, United States; Department of Materials Science and Chemical Engineering, State University of New York at Stony Brook, Stony Brook, New York 11794-2275, United States;* orcid.org/0000-0001-8518-1047

Complete contact information is available at:
https://pubs.acs.org/10.1021/acsphyschemau.1c00044

Notes

The authors declare no competing financial interest.

■ REFERENCES

(1) Zhao, B.; Ran, R.; Liu, M.; Shao, Z. A comprehensive review of $Li_4Ti_5O_{12}$-based electrodes for lithium-ion batteries: The latest advancements and future perspectives. *Mater. Sci. Eng., R Rep.* **2015**, *98*, 1−71.

(2) Yan, H.; Zhang, D.; Qilu; Duo, X.; Sheng, X. A review of spinel lithium titanate ($Li_4Ti_5O_{12}$) as electrode material for advanced energy storage devices. *Ceram. Int.* **2021**, *47*, 5870−5895.

(3) Fatima, H.; Zhong, Y.; Wu, H.; Shao, Z. Recent advances in functional oxides for high energy density sodium-ion batteries. *Mater. Rep., Energy* **2021**, *1*, 100022.

(4) Salvatore, K. L.; Lutz, D. M.; Guo, H.; Yue, S.; Gan, J.; Tong, X.; Liu, P.; Takeuchi, E. S.; Takeuchi, K. J.; Marschilok, A. C.; Wong, S. S. Solution-Based, Anion-Doping of $Li_4Ti_5O_{12}$ Nanoflowers for Lithium-Ion Battery Applications. *Chem. − Eur. J.* **2020**, *26*, 9389−9402.

(5) Sun, L.; Liu, Z.; Wang, Z.; Yang, W.; Yang, J.; Sun, K.; Chen, D.; Liu, Y.; Liu, X. The synergic effects of Ca and Sm co-doping on the crystal structure and electrochemical performances of $Li_{4-x}Ca_xTi_{5-x}Sm_xO_{12}$ anode material. *Solid State Sci.* **2019**, *87*, 110−117.

(6) Zhang, P.; Huang, Y.; Jia, W.; Cai, Y.; Wang, X.; Guo, Y.; Jia, D.; Sun, Z.; Wang, R.; Tang, X.; Wang, L. High rate capability of lithium chromium titanium oxide hierarchical mesoporous microspheres anode materials synthesized by a one-pot co-precipitation for lithium ion batteries. *J. Electrochem. Soc.* **2016**, *163*, A1920−A1920.

(7) Liu, Z.; Sun, L.; Yang, W.; Yang, J.; Han, S.; Chen, D.; Liu, Y.; Liu, X. The synergic effects of Na and K co-doping on the crystal structure and electrochemical properties of $Li_4Ti_5O_{12}$ as anode material for lithium ion battery. *Solid State Sci.* **2015**, *44*, 39−44.

(8) Zhang, Q.; Lu, H.; Zhong, H.; Yan, X.; Ouyang, C.; Zhang, L. W^{6+} & $Br^−$ codoped $Li_4Ti_5O_{12}$ anode with super rate performance for Li-ion batteries. *J. Mater. Chem. A* **2015**, *3*, 13706−13716.

(9) Wang, Z.; Yang, W.; Yang, J.; Zheng, L.; Sun, K.; Chen, D.; Sun, L.; Liu, X. Tuning the crystal and electronic structure of $Li_4Ti_5O_{12}$ via Mg/La Co-doping for fast and stable lithium storage. *Ceram. Int.* **2020**, *46*, 12965−12974.

(10) Shi, W.; Zhang, Z.; Qin, J.; Zhang, Y.; Liu, Y.; Liu, Y.; Gao, H.; Mao, Y. Interface modification by up-conversion material of Ho^{3+}-Yb^{3+}-Li^+ tri-doped TiO_2 to improve the performance of perovskite solar cells. *J. Alloys Compd.* **2018**, *754*, 124−130.

(11) Rajendran, S.; Thangavel, N. K.; Alkatie, S.; Ding, Y.; Arava, L. M. R. Y, Gd, and Pr tri-doped perovskite-type proton conducting electrolytes with improved sinterability and chemical stability. *J. Alloys Compd.* **2021**, *870*, 159431−159431.

(12) Deng, J.; Xu, Y.; Xiong, L.; Li, L.; Sun, X.; Zhang, Y. Improving the fast discharge performance of high-voltage $LiNi_{0.5}Mn_{1.5}O_4$ spinel by Cu^{2+}, Al^{3+}, Ti^{4+} tri-doping. *J. Alloys Compd.* **2016**, *677*, 18−26.

(13) Wang, L.; Zhang, Y.; Guo, H.; Li, J.; Stach, E. A.; Tong, X.; Takeuchi, E. S.; Takeuchi, K. J.; Liu, P.; Marschilok, A. C.; Wong, S. S. Structural and Electrochemical Characteristics of Ca-Doped "Flower-like" $Li_4Ti_5O_{12}$ Motifs as High-Rate Anode Materials for Lithium-Ion Batteries. *Chem. Mater.* **2018**, *30*, 671−684.

(14) Wang, L.; Zhang, Y.; McBean, C. L.; Scofield, M. E.; Yin, J.; Marschilok, A. C.; Takeuchi, K. J.; Takeuchi, E. S.; Wong, S. S. Understanding the Effect of Preparative Approaches in the Formation of "Flower-like" $Li_4Ti_5O_{12}$—Multiwalled Carbon Nanotube Composite Motifs with Performance as High-Rate Anode Materials for Li-Ion Battery Applications. *J. Electrochem. Soc.* **2017**, *164*, A524−A534.

(15) Deng, H.; Liang, W.; Nie, D.; Wang, J.; Gao, X.; Tang, S.; Liu, C.; Cao, Y.-C. High Rate Performance of Ca-Doped $Li_4Ti_5O_{12}$ Anode Nanomaterial for the Lithium-Ion Batteries. *J. Nanomater.* **2018**, *2018*, 7074824.

(16) Zhang, Q.; Zhang, C.; Li, B.; Kang, S.; Li, X.; Wang, Y. Preparation and electrochemical properties of Ca-doped $Li_4Ti_5O_{12}$ as anode materials in lithium-ion battery. *Electrochim. Acta* **2013**, *98*, 146−152.

(17) Cai, Y.; Huang, Y.; Jia, W.; Zhang, Y.; Wang, X.; Guo, Y.; Jia, D.; Pang, W.; Guo, Z.; Wang, L. Two-dimensional dysprosium-modified bamboo-slip-like lithium titanate with high-rate capability and long cycle life for lithium-ion batteries. *J. Mater. Chem. A* **2016**, *4*, 17782−17790.

(18) Ding, K.; Zhao, J.; Zhou, J.; Zhao, Y.; Chen, Y.; Zhang, Y.; Wei, B.; Wang, L.; He, X. Preparation and characterization of Dy-doped lithium titanate ($Li_4Ti_5O_{12}$). *Int. J. Electrochem. Sci.* **2016**, *11*, 446−458.

(19) Li, Y.; Wang, Z.; Zhao, D.; Zhang, L. Gd doped single-crystalline $Li_4Ti_5O_{12}/TiO_2$ nanosheets composites as superior anode material in lithium ion batteries. *Electrochim. Acta* **2015**, *182*, 368−375.

(20) Zhang, Q.; Verde, M. G.; Seo, J. K.; Li, X.; Meng, Y. S. Structural and Electrochemical Properties of Gd-Doped $Li_4Ti_5O_{12}$ as Anode Material with Improved Rate Capability for Lithium-Ion Batteries. *J. Power Sources* **2015**, *280*, 355−362.

(21) Xu, G. B.; Yang, L. W.; Wei, X. L.; Ding, J. W.; Zhong, J. X.; Chu, P. K. Highly-crystalline ultrathin gadolinium doped and carbon-coated $Li_4Ti_5O_{12}$ nanosheets for enhanced lithium storage. *J. Power Sources* **2015**, *295*, 305−313.

(22) Bai, Y.-J.; Gong, C.; Lun, N.; Qi, Y.-X. Yttrium-modified $Li_4Ti_5O_{12}$ as an effective anode material for lithium ion batteries with outstanding long-term cyclability and rate capabilities. *J. Mater. Chem. A* **2013**, *1*, 89−96.

(23) Chen, W.; Kuang, S.; Liu, Z.; Fu, H.; Yun, Q.; Xu, D.; Hu, H.; Yu, X. Y-doped $Li_4Ti_{5-x}Y_xO_{12}$ with $Y_2Ti_2O_7$ surface modification anode materials: Superior rate capability and ultra long cyclability for half/full lithium-ion batteries. *J. Alloys Compd.* **2020**, *835*, 155327−155327.

(24) Yang, X.; Yang, L.; Lin, S.; Zhou, R. Investigation on properties of $Pd/CeO_2-ZrO_2-Pr_2O_3$ catalysts with different Ce/Zr molar ratios and its application for automotive emission control. *J. Hazard. Mater.* **2015**, *285*, 182−189.

(25) Ngamou, P. H. T.; Ivanova, M. E.; Herwartz, C.; Lühmann, N.; Besmehn, A.; Meulenberg, W. A.; Mayer, J.; Guillon, O. Tailoring the structure and gas permeation properties of silica membranes via binary metal oxides doping. *RSC Adv.* **2015**, *5*, 82717−82725.

(26) Sathish, M.; Viswanathan, B.; Viswanath, R. P.; Gopinath, C. S. Synthesis, Characterization, Electronic Structure, and Photocatalytic Activity of Nitrogen-Doped TiO_2 Nanocatalyst. *Chem. Mater.* **2005**, *17*, 6349−6353.

(27) Fang, Q.; Meier, M.; Yu, J. J.; Wang, Z. M.; Zhang, J. Y.; Wu, J. X.; Kenyon, A.; Hoffmann, P.; Boyd, I. W. FTIR and XPS investigation of Er-doped SiO_2-TiO_2 films. *Mater. Sci. Eng., B* **2003**, *105*, 209−213.

(28) Abdel-wahab, M. S.; Jilani, A.; Yahia, I. S.; Al-Ghamdi, A. A. Enhanced the photocatalytic activity of Ni-doped ZnO thin films: Morphological, optical and XPS analysis. *Superlattices Microstruct.* **2016**, *94*, 108−118.

(29) Bard, A. J.; Faulkner, L. R. Fundamentals and applications. *Electrochem. Methods* **2001**, *2*, 580−632.

(30) Guo, Q.; Wang, Q.; Chen, G.; Shen, M.; Li, B. Molten Salt Synthesis of Different Ionic Radii Metallic Compounds Doped Lithium Titanate Used in Li-Ion Battery Anodes. *Mater. Trans.* **2017**, *58*, 383−389.